ATLAS NOTE

ATL-LARG-PUB-2015-001

17th July 2015

Upgrade plans for the Hadronic Endcap Calorimeter of ATLAS for the high luminosity stage of the LHC

Faig Ahmadov[a], Teresa Barillari[b], Mircea Cadabeschi[c], Alexander Cheplakov[a], Ruben Dominguez[d], Alexander Fischer[b], Jörg Habring[b], Armen Hambarzumjan[b], Namig Javadov[a], Andrey Kiryunin[b], Leonid Kurchaninov[e], Roy Langstaff[e], Mark Lenckowski[e], Sven Menke[b], Ignacio Molinas Conde[b], Martin Nagel[b], Horst Oberlack[b], Michel Raymond[f], Olaf Reimann[b], Peter Schacht[b], Pavol Strizenec[g], Sven Vogt[b], Giselher Wichmann[b]

[a]*JINR, Dubna, Russia*
[b]*Max-Planck-Institut für Physik, München, Germany*
[c]*University of Toronto, Canada*
[d]*University of Arizona, USA*
[e]*TRIUMF, Canada*
[f]*CERN, Switzerland*
[g]*Slovak Academy of Science, Kosice, Slovak Republic*

Abstract

The expected increase of the instantaneous luminosity of a factor seven and of the total integrated luminosity by a factor $3 - 5$ at the second phase of the upgraded high luminosity LHC compared to the design goals for LHC makes it necessary to re-evaluate the radiation hardness of the read-out electronics of the ATLAS Hadronic Endcap Calorimeter. The current cold electronics made of GaAs ASICs have been tested with neutron and proton beams to study their degradation under irradiation and the effect it would have on the ATLAS physics programme. New, more radiation hard technologies which could replace the current amplifiers have been studied as well: SiGe bipolar, Si CMOS FET and GaAs FET transistors have been irradiated with neutrons and protons with fluences up to ten times the total expected fluences for ten years of running of the high luminosity LHC. The performance measurements of the current read-out electronics and potential future technologies and expected performance degradations under high luminosity LHC conditions are presented.

1 Introduction

The expected increase in instantaneous and integrated luminosities of the second phase of the LHC upgrade to high-luminosities (HL-LHC) [1] may lead to the degradation of the ATLAS hadronic endcap (HEC) read-out electronics and thus to a degraded performance of the calorimeter. The degradation of the HEC read-out electronics under irradiation with protons and neutrons has been measured. This note summarizes these measurements and the expected impact on ATLAS physics at the HL-LHC. Alternative options have also been evaluated and are presented for comparison. Further options concerning the replacement of the ATLAS forward calorimeter (FCal) and the insertion of a smaller so-called Mini-FCal in front of the current FCal are discussed elsewhere [1, 2].

The note is organized as follows: in Section 2 the expected radiation levels at the location of the HEC electronics are discussed. Section 3 contains results of the irradiation tests of the current read-out electronics of the HEC. Possible ageing effects are discussed in Section 4 and the impact of the degraded electronics on ATLAS physics is summarized in Section 5. The results of irradiation tests of technologies which could potentially be used to replace the current electronics are shown in Section 6. Section 7 discusses the engineering and installation efforts needed for the exchange of the HEC read-out electronics.

2 Expected Radiation Levels in the Region with HEC Cold Electronics

The cold amplifiers for the Hadronic Endcap Calorimeter [3] of the ATLAS Experiment [4] have been designed to withstand ten years of operation of the LHC at a center of mass energy of $\sqrt{s} = 14\,\text{TeV}$ with peak luminosities of $\mathcal{L} = 10^{34}\,\text{cm}^{-2}\,\text{s}^{-1}$, corresponding to an integrated luminosity of $\int \mathcal{L}\,\text{d}\,t = 1000\,\text{fb}^{-1}$. They are located at the outer circumference of the HEC wheels inside the cryostat, in the region $432\,\text{cm} < |z| < 600\,\text{cm}$ and radius $r \simeq 204\,\text{cm}$[1].

To evaluate particle fluxes through the region with HEC cold electronics and corresponding radiation doses, dedicated simulations with different packages, developed by the ATLAS collaboration, have been carried out:

1. The application for the cavern background simulation [5] uses the GEANT toolkit [6] for detector description and the FLUKA code [7] for simulations of particle transport and interactions in matter. A simplified geometry of the ATLAS detector (where most of its parts are described as homogeneous volumes of a tube or cone shape) is used in this package. For the purposes of these studies, the description of the electromagnetic and hadronic endcap calorimeters was significantly modified to provide a more realistic distribution of materials in front of the region with HEC cold electronics. Radiation parameters were obtained in so-called scoring volumes – a grid of tubes in z and r with size $\Delta z \times \Delta r = 1 \times 1\,\text{cm}^2$. The input to the simulations were events from proton-proton-interactions at $\sqrt{s} = 14\,\text{TeV}$, generated with PHOJET [8]. In total, 29150 fully simulated events were analysed.

2. The standard ATLAS simulation framework [9] employs GEANT4 for the full simulation of the ATLAS detector. It contains a very detailed description of sub-detectors and services. But at the outer periphery of ATLAS not all services (power supplies and cables for example) are implemented. For this work, scoring volumes of size $\Delta z \times \Delta r = 1 \times 1\,\text{cm}^2$ were introduced in the HEC cold

---

[1] ATLAS uses a right-handed coordinate system with the x-axis pointing to the centre of the LHC ring, the y-axis in the vertical direction, the z-axis along the beam direction and $r = \sqrt{x^2 + y^2}$.

electronics region. The QGSP_BERT_HP [10] physics list, which includes high-precision treatment of low-energy neutrons, was selected for the simulations. Input events were generated with PYTHIA8 [11]. In total 99450 events were fully simulated.

3. The simulations described above can be compared with the outcome of the work of the ATLAS radiation background task force [12]. This is based on simulations performed in 2003, using the GEANT3 package [13] with the GCALOR code [14] for the hadronic shower development. A simplified description of the detector geometry for simulations was used and results were made available for a $\Delta z \times \Delta r$ granularity of $4 \times 4\,\mathrm{cm}^2$.

The expected Total Ionization Dose (TID) and $1\,\mathrm{MeV}$ neutron fluence (NIEL) in silicon obtained with the three different simulation packages are shown in Figure 1. It can be seen that the FLUKA based simulation predicts a $\simeq 30\%$ larger NIEL compared to GEANT4 over most of the $|z|$ range, with the exception of the region $|z| > 550\,\mathrm{cm}$ where the missing service parts in the standard ATLAS simulation cause a rise in NIEL, and the front most region with the largest NIEL, where the two simulations agree. The older GEANT3 based simulation predicts $\simeq 50\%$ larger NIEL values for $|z| < 500\,\mathrm{cm}$ compared to FLUKA and approaches the FLUKA result for larger $|z|$. For TID the situation for FLUKA and GEANT4 is similar: FLUKA results are up to $\simeq 50\%$ above the GEANT4 results for $|z| < 500\,\mathrm{cm}$ and the GEANT4 predictions rise above the FLUKA predictions for $|z| > 550\,\mathrm{cm}$. The GEANT3 predictions are $\simeq 50\%$ lower for TID than those from FLUKA for all $|z|$. In general, there is a rather good agreement between the different simulations and a safety factor of 2 on top of the FLUKA predictions can account for all observed variations.
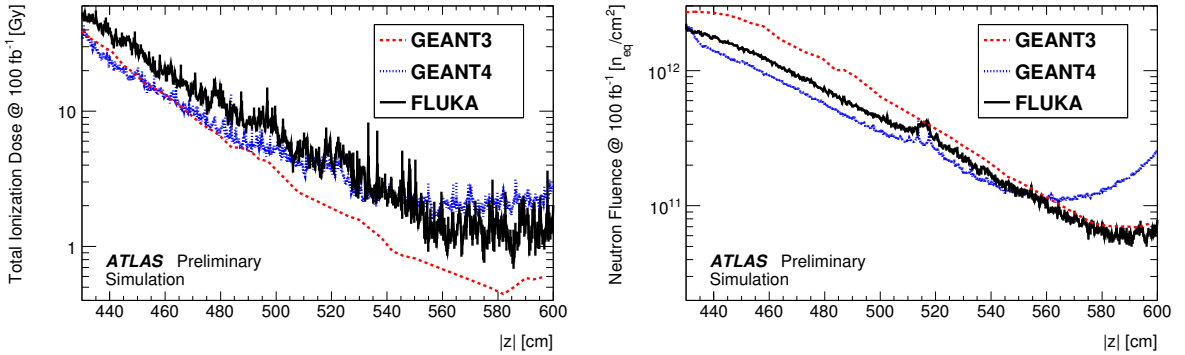

Figure 1: Expected radiation levels for TID (left) and NIEL (right) in silicon at the location of the HEC cold electronics for three different simulations. The values correspond to one standard LHC year at $\sqrt{s} = 14\,\mathrm{TeV}$ with an integrated luminosity of $100\,\mathrm{fb}^{-1}$ and without any safety factors applied. The red curve shows the older GEANT3 results, while the blue and black curve show more recent GEANT4 and FLUKA results, respectively.

For integrated luminosities of $3000\,\mathrm{fb}^{-1}$ a maximum of $3.1\,\mathrm{kGy}$ of total ionization dose (TID) in silicon are expected from FLUKA, including the safety factor of 2, while the corresponding number for the $1\,\mathrm{MeV}$ equivalent neutron fluence (NIEL) in silicon is $1.2 \times 10^{14}\,\mathrm{n_{eq}/cm^2}$. Figure 2 shows the expected ATLAS Si-NIEL fluences induced in the ASICs as a function of the location of the read-out cell in the HEC detector which will be read out by the corresponding ASIC.
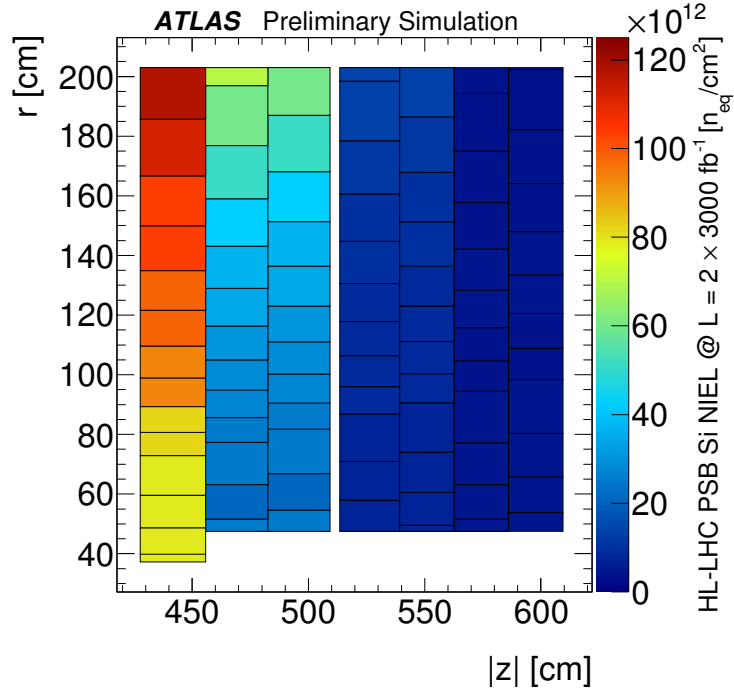
3

Figure 2: Silicon NIEL fluence in ATLAS under HL-LHC conditions after $3000\,\mathrm{fb}^{-1}$ and with an applied safety factor of 2 to account for simulation uncertainties. The color coded fluences in the Pre-amplification and Summing Boards (PSB) carrying the ASICs are shown at the $r-z$ locations of the regions in the HEC they read out. The front-most vertical section corresponds to the first read-out layer while adjacent pairs of vertical sections are summed for the three remaining read-out layers. Blocks belonging to the same read-out channel are therefore shown with the same fluence.

3 Irradiation Tests

Proton and neutron irradiation tests have been performed to evaluate the limits of the current read-out electronics under HL-LHC conditions [15].

In addition to the in situ measurements during the irradiation which took place at room temperature, the neutron irradiated boards were re-tested three months after the neutron tests, immersed in liquid nitrogen to simulate the conditions inside the ATLAS endcap cryostat where the read-out electronics of the HEC are located.

3.1 Proton Tests

A $198.9\,\mathrm{MeV}$ proton beam of $2.71\,\mathrm{nA}$ at the Proton Irradiation Facility (PIF) at PSI, Switzerland with a narrow beam profile of $\sigma_x \simeq 7\,\mathrm{mm}$ and $\sigma_y \simeq 9\,\mathrm{mm}$ at the position of the devices under test was used in 2011 to evaluate the radiation hardness against hadrons up to a fluence of $2.6 \times 10^{14}\,\mathrm{p/cm^2}$ after $22.05\,\mathrm{h}$ of beam time. A mount with 14 equidistant slots with a slot spacing of $1.7\,\mathrm{cm}$ were placed in the beam line. The six boards closest to the beam window housed transistors in SiGe bipolar and Si CMOS FET technology and the GaAs FET based ASICs (BB96) [16]. The BB96 ASICs are currently used in ATLAS for the HEC read-out. Slots 7 and 14 were equipped with radiation diodes for dose measurements, and

slots $8 - 13$ with test structures for the HEC power supplies. A picture of the setup prior to final alignment is shown in Figure 3.
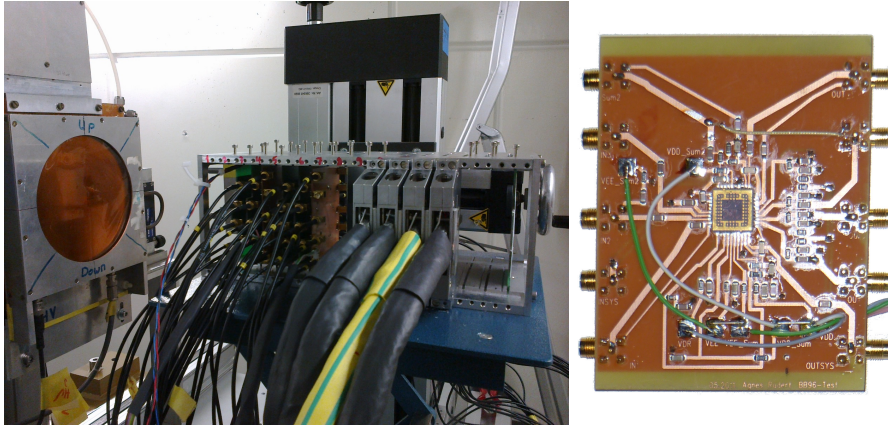

Figure 3: Picture of the test setup at PSI prior to final positioning (left). The proton beam comes from the left. An ionization chamber is visible as a large aluminum square with a round hole on the left hand side. The test boards for the HEC read-out electronics (right) are mounted in the first 6 slots of the aluminum frame in the picture center.

The beam position and width were measured with sheets of EBT2 radiation film [17] placed for 5 minutes in the beam behind 6 different slots. The total beam flux was measured and calibrated by the PIF group with ionization chambers. The raw ionization chamber current measurements in 1 s intervals and the conversion factor to the proton beam current were used to calculate the accumulated proton charge as a function of time. Together with the beam width and position measurements from the radiation films the fluence for the devices under test in each slot was derived. The alignment of the setup was done prior to irradiation by means of two lasers indicating the horizontal and vertical planes containing the beam direction. The laser system was however misaligned for the horizontal plane which led to an offset of (6.5 ± 0.5) mm in y, while the positioning of the boards themselves limited the precision in x to about ± 1 mm. Taking into account the small variations of the beam profile along the beam line, the offset of the beam in y, and the expected losses due to nuclear reactions in the devices under test, the flux was found to be the same for all slots.

Figure 4 shows the horizontal and vertical profiles of the proton beam as measured by one of the radiation films. Dips in the data distribution are caused by the soldered legs of housings in the upstream slots. The superimposed Gaussian fits in all films show that the profiles are roughly Gaussian in the area of the ASICs.

3.2 Neutron Tests

Neutron tests were performed in 2012 with a $12 - 14 \, \mu A$ and 36 MeV proton beam of the variable-energy cyclotron U-120 at NPI in Řež, Czech Republic, hitting a 16 mm thick D_2O target to produce a neutron spectrum with $E_{kin} < 32$ MeV and $\langle E_{kin} \rangle \simeq 14$ MeV [18]. Similar to the setup in the proton test, 16 equidistant slots with distances of 1.7 cm between adjacent board centers were equipped and placed in front of the 3 mm steel plate enclosing the target. The alignment was done prior to mounting the target and the test boards by burning small holes with the proton beam in two calibration boards placed instead of the test structures in the first and last slot. Slots 1–6, 8, and 9 were equipped with the BB96 GaAs ASICs,
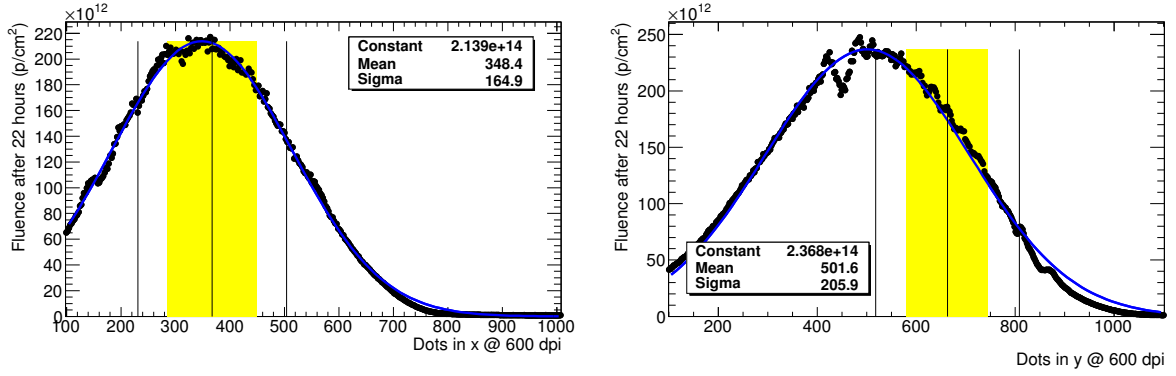
Figure 4: Horizontal (left) and vertical (right) profiles of the proton beam at PIF behind slot 3, normalized to the total fluence after 22 hours of beam time. The data points indicate the measurements from the radiation film. Superimposed are Gaussian fits. The yellow bands depict the position of the ASIC and the vertical lines the center and boundaries of the housing. The film was scanned with a resolution of 600 dots per inch (dpi). The Gaussian parameters for mean and width are also given in dpi.

slots 7 and 11 with radiation diodes and activation foils and the remaining slots with test structures for the HEC power supplies. The setup is shown in Figure 5.
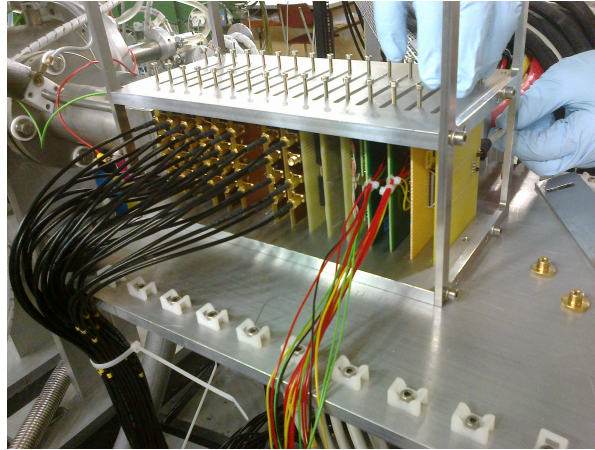

Figure 5: Picture of the test setup at NPI. The neutrons leave the D_2O target at the upper left part of the picture and travel to the right. The test boards for the HEC read-out electronics occupy the first 6 slots and slots 8 and 9 of the aluminum frame in the picture center.

The total collected proton charge in the test was 2.0 C. The neutron flux profile was measured with sheets of EBT2 radiation film placed for 5 minutes at a reduced machine current of $1.2\,\mu A$ in front of slot 1 and behind all other slots with the exception of slots 7,10, and 11. During a dedicated fluence test run in 2010 with radiation monitors in each slot the following empirical relation of the 1 MeV equivalent neutron fluence in silicon and the integrated machine current as function of the slot number was found [19]:

$$\text{fluence} = \frac{1.61 \times 10^{10}\,\text{n}_{\text{eq}}}{\text{cm}^2\mu C} \left(\text{slot} + \frac{\text{offset} \pm 2\,\text{mm}}{17\,\text{mm}}\right)^{-2.11}, \tag{1}$$

6

where slot is the slot-number (1-16), offset is the distance of the first slot from the target (3 mm) and the positions are known with ±2 mm precision.
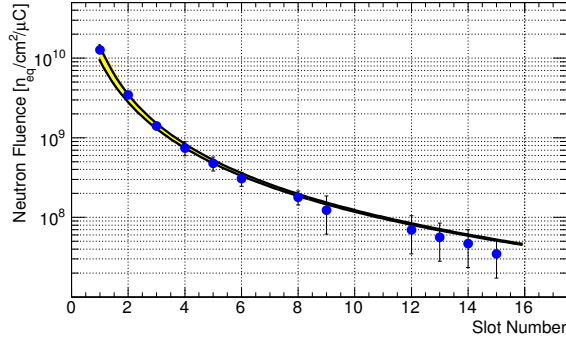

Figure 6: 1 MeV equivalent neutron fluence in silicon as function of slot number normalized to the integrated machine current. The data points depict relative dose measurements from radiation films normalized to the expected fluence in slot 3. The band between the two solid lines corresponds to the fluence curve measured in 2010 in a dedicated run with radiation monitors in each slot.

Figure 6 shows this fluence curve superimposed with the relative fluence measurements from the radiation films, normalized to the expected fluence in slot 3.

3.3 S-Parameter Measurements

During the irradiation the scattering parameters (S-parameters) [20] of the BB96 ASICs were continuously measured to study their performance as a function of fluence. S-parameters describe the electrical behavior of a linear electrical network in the frequency domain. The S-parameters were measured for the frequency range 300 kHz to 100 MHz with a vector network analyzer (VNA) connected via 40 m long cables to the devices under test. Each cable pair was individually de-embedded with the VNA calibration utility [21] moving the plane of calibration to the input connectors of the boards. The most important parameters are the input port reflection coefficient S_{11}, which can be translated into the input impedance $Z_{in} = 50\,\Omega\,(1 + S_{11})/(1 - S_{11})$ for the case of vanishing feedback coefficient S_{12} and low load reflection, and the forward transmission coefficient S_{21}. The product of the two gives the transimpedance gain in the frequency domain. This can be interpreted as the input current to output voltage signal amplification. It was found that the effect of protons in the GaAs ASICs is similar to that of neutrons with ~5 times larger fluence. Since the expected ratio of neutron to proton fluence for the HL-LHC is ~10 [1], the neutron tests provide the most limiting numbers.

3.4 Pulse Measurements

In the neutron test triangular voltage pulses similar to the ionization currents in the LAr gaps in ATLAS with 10 different amplitudes between 0.7 mV and 70 mV and pulse lengths of 500 ns were applied over the 40 m cables at the BB96 ASICs, and both the input and the output pulse were measured with an oscilloscope (the output pulse again after a 40 m cable). These measurements were done alternately with the S-parameter measurements and provide a more direct way of studying the performance of the electronics. Good agreement with the S-parameter measurements was found for the gain as a function of

7

neutron fluence. The largest expected ionization currents in ATLAS are $250\,\mu A$ for a single pre-amplifier (PA) and about $500\,\mu A$ for a full chain of several PAs and one summing amplifier or driver. Up to these values the linearity of the PAs and the full system was measured with pulses. To convert from input voltage pulses to currents the input impedance and cable damping was taken into account. The voltage range of $0.7\,mV$ to $70\,mV$ corresponds to an input current range of $10\,\mu A$ to $1000\,\mu A$ for non-irradiated chips.

3.5 Warm in Situ Results

The forward transmission coefficient normalized to the value before irradiation and evaluated in the frequency range of the shaper electronics in ATLAS ($4\,MHz < f < 10\,MHz$) as measured in situ for the full systems consisting of one PA and a summing amplifier during the proton and neutron irradiations is shown in Figure 7 as function of the proton and 1 MeV equivalent neutron fluence in silicon. Figure 7
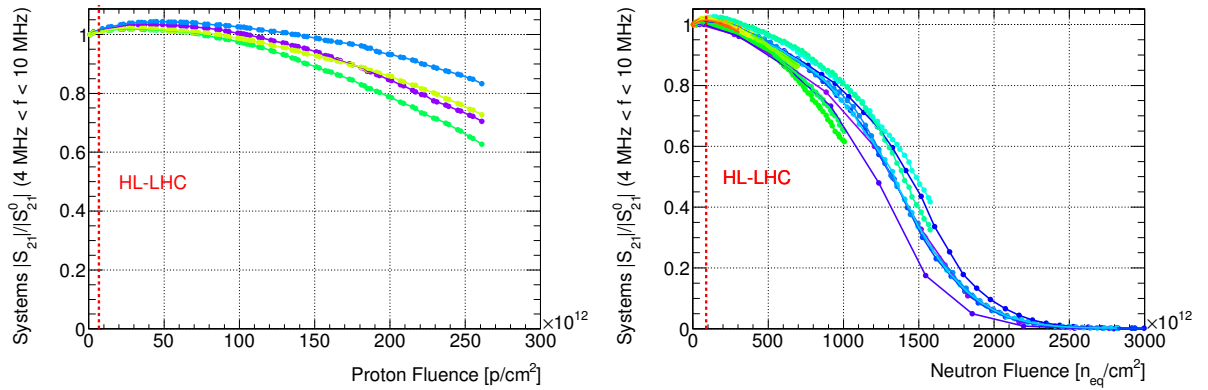

Figure 7: Forward transmission coefficient normalized to the value before irradiation and evaluated in the frequency range of the shaper electronics in ATLAS ($4\,MHz < f < 10\,MHz$) as measured in situ for a system of PA and summing amplifier during the proton (left) and neutron (right) irradiations versus the fluence. The neutron fluence is given in 1 MeV equivalent for silicon as measured in Řež. The red vertical lines indicate HL-LHC limits including a safety factor of 2. In the proton case the limit assumes all damage would be due to TID of the protons (neglecting NIEL). In the neutron case the fluence limit is corrected by the expected differences in GaAs (see Section 3.7). The colored data points are from the various devices under test and the spread of the points indicate sample variations. Since for the neutron test the fluence varied with slot number the point density and maximal fluence per slot varies.

shows that the device-to-device fluctuations increase with irradiation and that the effect of protons is about $4-5$ times larger on the voltage gain compared to that of neutrons at the same fluence values. Input impedances were found to stay close to $50\,\Omega$ and are real throughout the entire irradiation range for protons and up to ~$4 \times 10^{14}\,n_{eq}/cm^2$ for neutrons. The output impedance shows similar behavior and stays close to $50\,\Omega$ roughly twice as long. Beyond these limits the impedances stay real but rise quickly resulting in non-matched conditions in ATLAS, where $0.5-2\,m$ $50\,\Omega$ cables connect the detector and the PAs and ~$10\,m$ $50\,\Omega$ cables carry the signals from the ASIC output to the shaper electronics.

3.6 Cold Results

About three months after the neutron irradiation tests at NPI in Řež the irradiated boards were shipped to the MPP lab in Munich and re-tested with the same set of measurements as in situ in both warm and

cold (liquid nitrogen) conditions. The three front-most boards received neutron fluences in excess of 2.8×10^{15} n_{eq}/cm^2 (Si 1 MeV eq. in Řež). From Figure 7 it can be seen that beyond 2.1×10^{15} n_{eq}/cm^2 the ASICs approach 0 voltage gain and therefore the three first boards were not functioning anymore. The board in the fourth slot was exposed to 1.6×10^{15} n_{eq}/cm^2 and this one plus the following four boards from slots 5,6,8, and 9, with respective fluences of 10.0, 6.9, 3.8, and 3.0×10^{14} n_{eq}/cm^2 were still operational in warm conditions and still showed the same performance as was measured at the end of the run in situ at Řež. In addition to these 5 fluence points non-irradiated ASICs have been measured in warm and cold as well to provide data at zero fluence. Immersed in liquid nitrogen to emulate the conditions inside
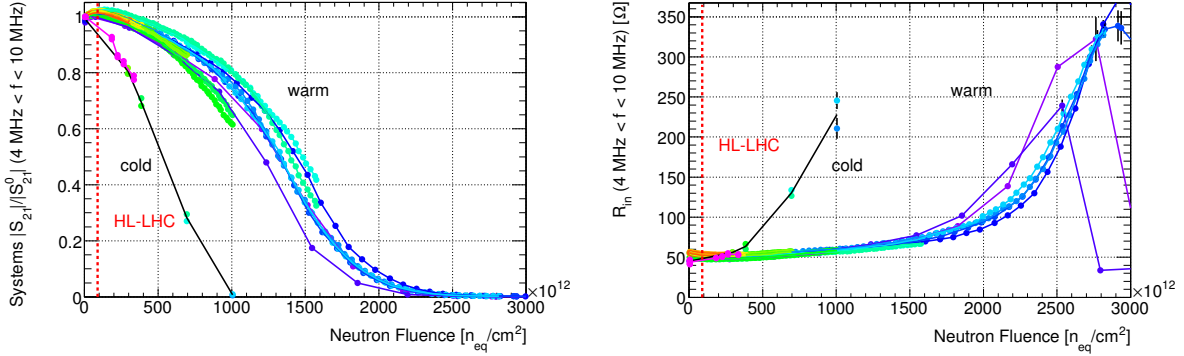

Figure 8: Forward transmission coefficient normalized to the value before irradiation (left) and input impedance (right) evaluated in the frequency range of the shaper electronics in ATLAS ($4\,\mathrm{MHz} < f < 10\,\mathrm{MHz}$) as measured in situ for systems of a PA and a summing amplifier during the neutron irradiations in warm and in cold three months after the irradiation versus the fluence. The neutron fluence is given in 1 MeV equivalent for silicon. The red vertical lines indicate the HL-LHC limit including a safety factor of 2.

the ATLAS cryostat, the performance is dramatically worse than in warm conditions. Figure 8 shows the normalized forward transmission coefficient and the input impedance for the systems comprised of one PA and a summing amplifier as function of neutron fluence for both warm and cold conditions. The sparse data points on the left indicate the cold measurements, while the denser groups of points extending to larger fluences are the measurements in warm. The performance in cold is roughly equivalent to that in warm at 3 times larger fluences. The performance degrades quickly beyond $3 - 4 \times 10^{14}$ n_{eq}/cm^2.

In order to understand the large temperature dependence in performance degradation for the BB96 ASIC the DC characteristics of the two types of transistors used in the ASIC (so called DFET and MFET) have been tested at room temperature and immersed in liquid nitrogen. Figure 9 shows these measurements compared to SPICE-simulations for the transistors. While the model parameter variations (indicated by the dashed lines) allow for a wide range of possible IV-curves, the measured and predicted curves show the same shift in threshold voltage by $\Delta V_{th} \simeq +0.4\,\mathrm{V}$ for both transistor types in the transition of warm to cold conditions.

In Figure 10 the threshold voltage V_{th} for both transistor types is shown as measured in situ (warm) during neutron irradiations at Řež. For a Si-NIEL fluence of $1 \cdot 10^{15}$ n_{eq}/cm^2 threshold voltage increases of 0.45 V (DFET) and 0.60 V (MFET) are observed, respectively. It can be concluded that the operation in cold has the same effect on the transistors as irradiating them with $6 - 8 \cdot 10^{14}$ n_{eq}/cm^2. The same offset of $6 - 8 \cdot 10^{14}$ n_{eq}/cm^2 can be observed in Figure 8 when warm and cold values for the forward transmission coefficient are compared.

The pulse measurements as described in Section 3.4 have also been repeated with the already irradiated
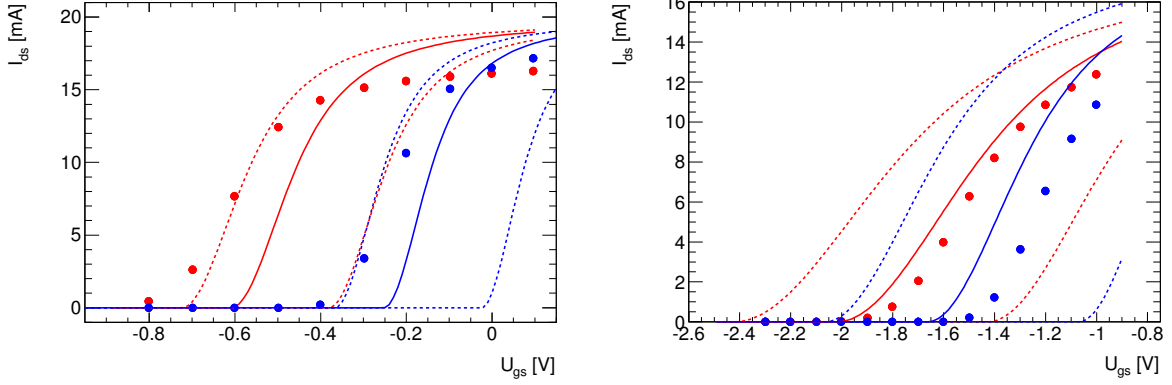
Figure 9: Drain-Source current of DFET (left) and MFET (right) transistors in warm (red) and cold (blue) versus the Gate-Source voltage for a small applied Drain-Source voltage (10 mV). The solid dots show measured data; solid lines are model predictions for default model parameters; dashed lines correspond to variations in the model parameters.
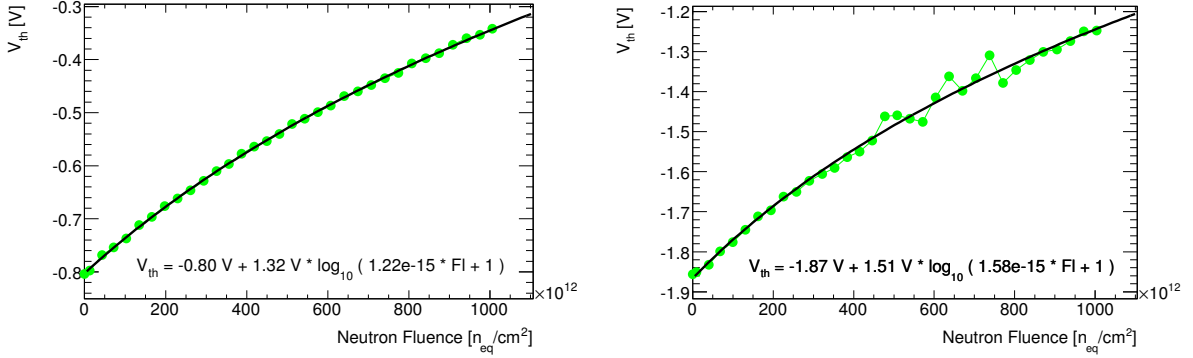

Figure 10: Threshold voltage V_{th} of DFET (left) and MFET (right) transistors in warm under neutron irradiation versus the neutron fluence. The solid dots show measured data; solid lines indicate a fit to a logarithmic function. The apparent fluctuations for the MFET around threshold voltages of -1.4 V are due to the small number of working points (step size 0.05 V) available during the measurements.

boards in warm and in cold. The pulse amplitudes have been adjusted to lower levels to still correspond to $10 - 1000 \, \mu A$ input currents for non-irradiated ASICs for the short (~4 m) cables used at MPP. The increase of non-linearity of the response was found to be described by a power-law relation of input (in) and output (out) amplitude of the form:

$$\text{out} = c \times \text{in}^x, \tag{2}$$

where c is a fluence-dependent constant and x the power-law exponent. Values for x deviating from 1.0 indicate non-linear behavior.

Figure 11 shows this exponent as function of neutron fluence in warm and cold. As in the case of the forward transmission coefficient the non-linearities for irradiated ASICs are worse in cold and correspond roughly to those in warm at 3 times larger fluences. Since up to 16 PAs are summed by one summing
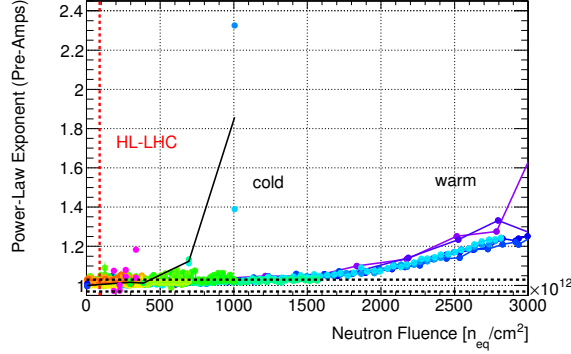
Figure 11: Measured non-linearity of the PAs as function of neutron fluence in warm (dense data points extending to large fluences) and in cold (sparse data points at lower fluences). The non-linearity is expressed in terms of a power-law exponent. Deviations from 1.0 indicate non-linear behavior. Horizontal dashed lines indicate exponent limits for a deviation of 1% from linear expectation of the output amplitude normalized to the maximum amplitude. The neutron fluence is given in 1 MeV equivalent for silicon. The red vertical line indicates the HL-LHC limit including a safety factor of 2.

amplifier in ATLAS the non-linearities for the PAs can not be corrected. An exponent of 1.03 or 0.97 would correspond to a maximum deviation of 1% of the output amplitude normalized to the maximum amplitude from linear expectation. This original requirement limit for the non-linearity of the PAs is indicated by the horizontal lines in Figure 11. Beyond neutron fluences of $3 - 4 \times 10^{14} \, \mathrm{n_{eq}/cm^2}$ the non-linearity quickly rises above this level.
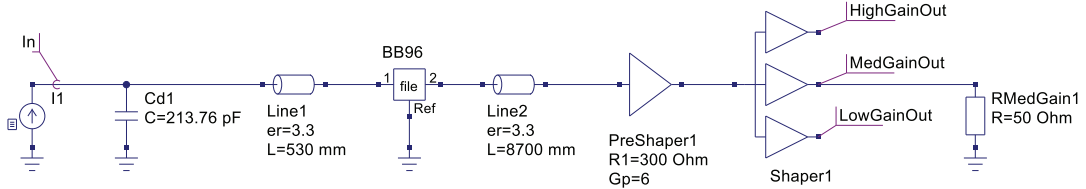

Figure 12: The full electronics chain for a typical HEC channel with detector capacitance $C_d = 213.76 \, \mathrm{pF}$ and a 530 mm coax cable between detector and ASIC. The ASIC (BB96 in the figure) is described by the measured S-parameters. The output is connected via a ~8.7 m coax cable to pre-shaper and shaper circuits. The typical medium gain amplification of the shaper is assumed.

The degraded S-parameter measurements in cold over the full frequency range of $300 \, \mathrm{kHz} - 100 \, \mathrm{MHz}$ have been used to predict the response to a typical ionization signal in the HEC after the full electronics chain for the HEC in ATLAS [22] (see Figure 12). Figure 13 shows the simulated response to a 400 ns triangular current in a typical HEC channel at four different fluence values. It can be seen that on top of the gain degradation the pulse shape worsens with increasing fluence leading to a slower rise- and fall-time, a broader and more delayed positive peak.
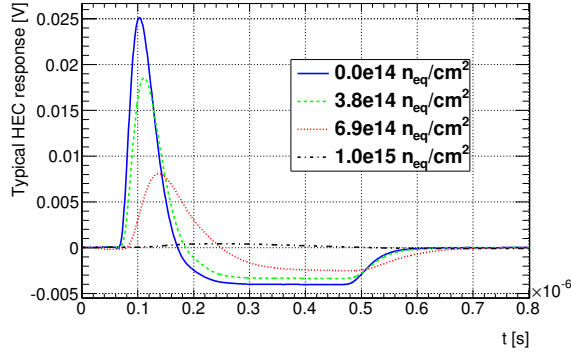
Figure 13: Simulated typical response in cold to a 400 ns triangular ionization current in the HEC for one channel for four different neutron fluences. The fluence is given as 1 MeV equivalent fluence in silicon for the neutron spectrum at NPI in Řež.

3.7 Fluence Conversion for GaAs

The neutron fluence values given in all figures presented so far (if not explicitly stated otherwise like in Figure 2) are 1 MeV equivalent fluences in silicon evaluated for the neutron spectrum at NPI in Řež [18]. In order to compare these values to expectations for the HL-LHC the fluences have to be converted for the GaAs devices studied here first to the corresponding 1 MeV equivalent fluence in GaAs using the NPI neutron spectrum and the Kerma factors for neutrons in silicon and gallium-arsenide [23–29]. In a second step, using the expected neutron, proton and pion spectra in ATLAS [12], the 1 MeV equivalent neutron fluence in GaAs has to be converted back to Si using Kerma factors for the relevant radiation in both Si and GaAs. It was found that the conversion from Si to GaAs at NPI energies is 1.82 and from GaAs to Si at the location of the ASICs in ATLAS 1/1.35. All measured neutron fluences at NPI reported here can thus be converted to ATLAS expectations by multiplying with 1.82/1.35.

4 BB96 Ageing Tests

Another aspect of the qualification of the HEC cold electronics for operation under HL-LHC conditions is the investigation of potential ageing effects on their performance. At the end of the HL-LHC operation, the BB96 ASICs will have been in operation under radiation for over 20 years. Since robust data about the long-term stability of electronic components in these conditions is not available, an effort was undertaken to accelerate the ageing process in the lab, and then look for performance degradation and signs of mechanical stress or damage of the electronic components.

4.1 Cold Ageing Test

The HEC read-out electronics are immersed in liquid argon inside the HEC cryostat and operating at 87K. To study ageing at cryogenic temperatures, four PCBs, each equipped with 2 pre-amplifiers and 2 sytems, were kept unpowered for 16 days inside a cryostat filled with liquid nitrogen, and various performance parameters of the ASICs were measured before and after the test: DC-values, S-parameters

Table 1: Relative performance degradation of BB96 ASICs after ≈16 days (386 hours) at -190° (unpowered). $\Delta|S_{21}|$ denotes the relative change in the forward transmission coefficient and $\Delta R_{in(out)}$ the relative changes in the real parts of input and output impedance, respectively.

ASIC	Correction for	$\Delta|S_{21}|$ (%)	ΔR_{in} (%)	ΔR_{out} (%)
	temperature only	-1.1 ± 0.4	1.5 ± 0.5	0.2 ± 0.1
Pre-Amps	temperature and light	-0.9 ± 0.4	1.2 ± 0.5	0.1 ± 0.1
	light only	-1.1 ± 0.4	1.7 ± 0.4	0.1 ± 0.1
	temperature only	-0.8 ± 0.4	1.6 ± 0.6	0.4 ± 0.3
Systems	temperature and light	-0.7 ± 0.4	1.2 ± 0.6	0.3 ± 0.3
	light only	-1.0 ± 0.4	1.7 ± 0.5	0.4 ± 0.3

(see Section 3.3), and the pulse response as described in Section 3.4. The left-hand side of Figure 14 shows a picture of the PCBs inside the cryostat.
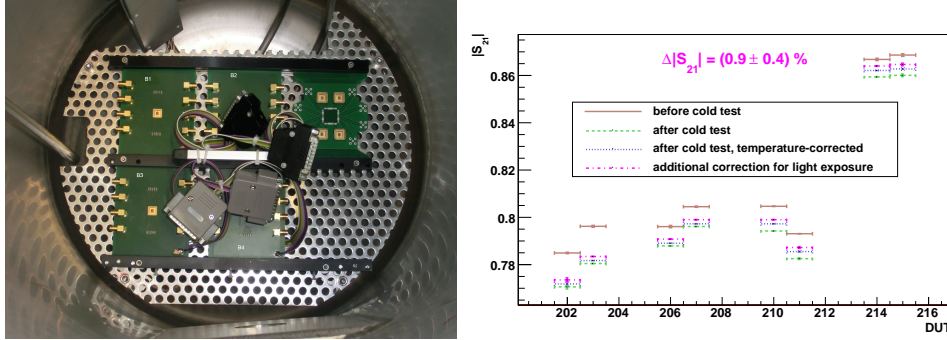

Figure 14: A picture of the four PCBs inside the cryostat (left), and a comparison of $|S_{21}|$ for all pre-amplifiers before and after the cold test, with several corrections applied (right). The abscissa indicates the number of the device under test (DUT).

Some minor differences between the measurements before and after the cold test complicate their comparison: there was a temperature difference between the two measurements ranging from $\Delta T = +0.70°$ to $\Delta T = +1.85°$, depending on the specific PCB; the chips were covered with a plastic lid before the test which was removed before putting them inside the cryostat; and after the cold test, a few channels were not working because of problems in the outer circuitry. To correct for these differences, some additional un-irradiated PCBs were used to study their temperature dependence and their response to light exposure, and an example of applying the resulting correction factors to the measurements is shown in the right-hand side of Figure 14 for $|S_{21}|$ of the pre-amplifiers. The results of the cold ageing test are reported in Table 1, with the various correction schemes yielding similar results. In summary, a small performance degradation of the order of 1% is observed after 16 days in liquid nitrogen. It is clear that this 1% degradation over a period of 16 days cannot simply be linearly extrapolated to longer time scales, since the BB96 ASICs currently in operation in the ATLAS detector do not show any degradation that would be compatible with such an assumption. The result is thus attributed either to an initial drop in performance after cooling down the ASICs or to some unknown systematic effect of the measurements.

Table 2: Relative performance degradation of BB96 ASICs after 86 temperature cycles between 5°C and 100°C (unpowered). The parameter definitions are the same as in Table 1.

ASIC	$\Delta |S_{21}|$ (%)	ΔR_{in} (%)	ΔR_{out} (%)
Pre-Amps	-0.3 ± 0.5	0.5 ± 0.6	0.0 ± 0.1
Systems	-0.2 ± 0.1	1.0 ± 1.5	0.0 ± 0.2

4.2 Warm Ageing Test

Another way to artificially accelerate the ageing process of electronic devices is to temperature-cycle them. A different set of four PCBs were exposed to 86 temperature cycles between +5°C and +100°C over a period of 14 days with each stage of constant or ramping temperature lasting for about an hour. The right-hand plot of Figure 15 compares the measurements of $|S_{21}|$ for the pre-amplifiers with the data taken prior to the temperature cycles (warm test). These comparisons are also shown in numerical form in Table 2. The results for all parameters are compatible with the observation of no performance degradation.
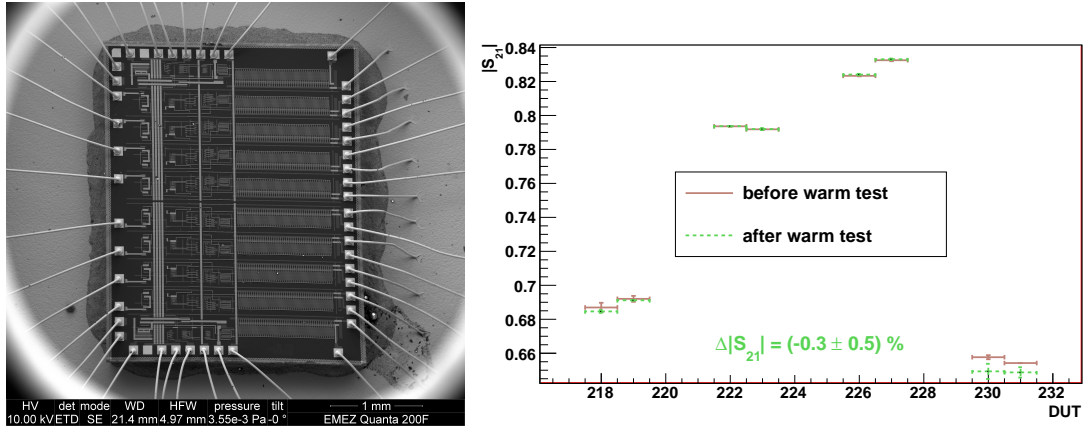

Figure 15: An electron microscope picture of one die packaged without lid onto a PCB, taken after the warm test (left), and a comparison of $|S_{21}|$ for all pre-amplifiers (DUT) before and after the warm test (right).

In addition to evaluating performance parameters, individual transistors were examined for signs of mechanical stress or damage after the warm test with both optical and electron microscopes. The electron microscope examination was performed at the ScopeM facility at the ETH Zürich, and the left-hand side of Figure 15 shows an example of the many electron microscope pictures that were taken. No signs of mechanical damage were visible after either the cold or the warm test. The material analysis performed supplementarily at ETH confirmed the material composition of the dies and was useful to exclude potential ageing problems from Al-Au junctions or inappropriate glue.

5 Impact of Degraded Electronics on ATLAS

The extrapolation of the performance of the read-out electronics shown in Figure 13 and described in Section 3.6 can be extended to other fluence values. The S-parameters have been interpolated between the measured values and parameterized as function of the fluence. The interpolated data sets have been used to predict the pulse shapes for these fluence values in different HEC read-out cells. For a typical HEC read-out cell the resulting pulse from the interpolation of S-parameters as function of time for various ATLAS Si-NIEL fluences in steps of $1.0 \times 10^{14}\,\mathrm{n_{eq}/cm^2}$ is shown in the left plot of Figure 16. The right plot in the same figure shows the autocorrelation function – the folded response to a delta-peak with itself – normalized to unit amplitude as function of the sample number (one sample is taken every 25 ns in ATLAS) for the same fluence values. The effective gain for an ionization signal is determined from the pulse amplitudes, but the full signal reconstruction in ATLAS uses the autocorrelation functions to calculate optimal filter weights in the digitization step. This is done in the simulation described in the next sections. Also the actual electronics noise could be simulated with the autocorrelation function but in ATLAS is taken from measured noise data instead – so the increase in noise due to degraded pulse shapes is not fully accounted for.
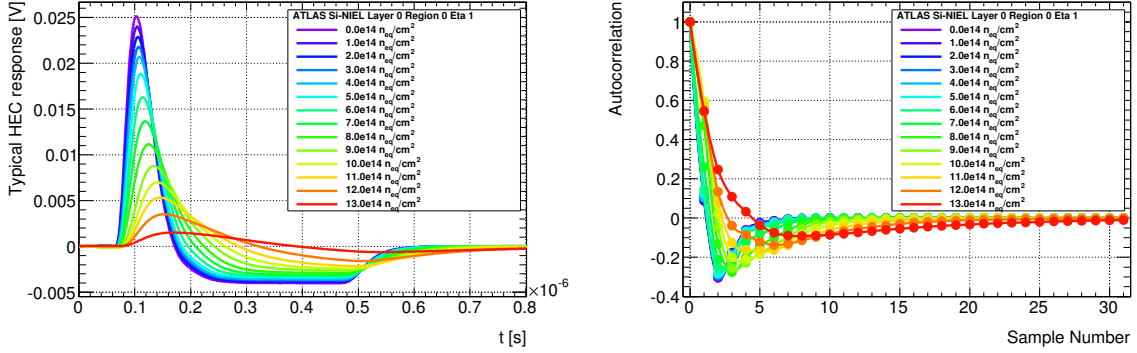

Figure 16: Simulated typical response (left) to a 400 ns triangular ionization current in the HEC and the corresponding autocorrelation function (right) for one channel for different NIEL fluences for silicon in ATLAS.

The increase of the non-linearity exponent x under irradiation can be modeled with a simple function of the form:

$$x = x_0 + \exp(c_0 + c_1 \times Fl), \tag{3}$$

where x_0, c_0, and c_1 are constants and Fl is the Si-NIEL fluence as measured in Řež. Figure 17 shows the exponent fit to the measured data points as function of Si-NIEL in Řež for the PAs alone (top left) and the systems (PA and driver) (top right). The bottom plot in the same figure shows the two fit functions compared to their ratio, which can be interpreted as the non-linearity of the driver stage alone. From the ratio it can be seen that most of the non-linear behavior stems from the pre-amplification, not the driver. The fitted values of the non-linearity exponent for the PAs are:

$$x_0 = 1 \quad \text{(fixed)}; \qquad c_0 = -5.64 \pm 0.63; \qquad c_1 = (5.46 \pm 0.91) \times 10^{-15}\,\mathrm{cm^2/n_{eq}}. \tag{4}$$
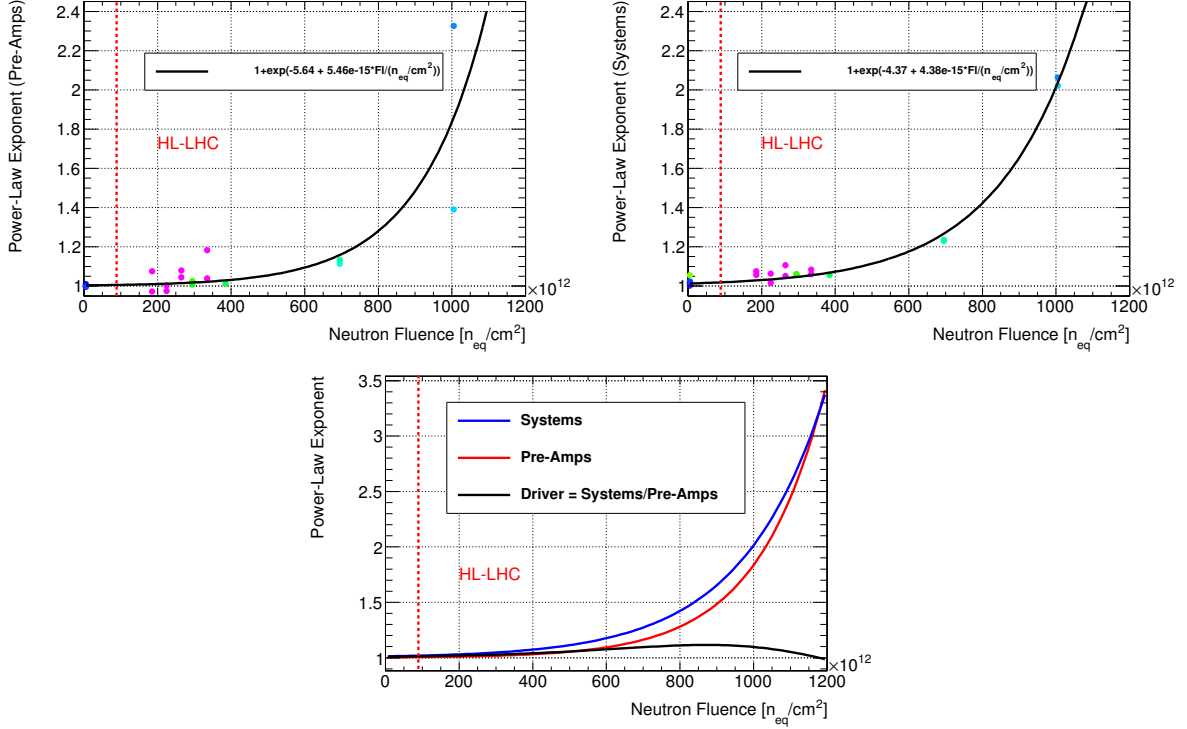
Figure 17: Non-linearity of the PAs as function of neutron fluence in cold for the PAs (top left) and the systems consisting of PA and driver (top right). Superimposed are fits to the data (constant plus exponential as in Eq. 3). Both fits and their ratio are shown in the bottom plot. The ratio can be interpreted as the non-linearity stemming from the driver stage. Thus the main contribution to the non-linearity originates in the PAs.

5.1 Parameterization of Degradation

A di-jet Monte Carlo sample was chosen to study the HEC performance degradation due to radiation damage. The PYTHIA [30] Monte Carlo generator was used to generate hard scattering $2\rightarrow2$ QCD processes with two leading jets in the intermediate p_T-range (140 GeV $< p_T <$ 280 GeV), overlapping at least partially with the HEC region (1.5 $< |\eta| <$ 3.2). ATLAS uses anti-k_T jets [31] with a distance parameter of $R = 0.4$ and thus the simulated η range to partially overlap with the HEC was chosen to be 1.1 $< |\eta| <$ 3.6. A total of 16300 di-jet events have been generated and fully simulated [9]. The simulated sample does not include any pile-up of pp collisions.

A dedicated event sample produced at the initial stage of the simulation (prior to the digitization and reconstruction procedures) contains the values of energy deposited in each HEC sub-gap in a given event. If no degradation is assumed, these initial values remain unchanged and enter the digitization and reconstruction procedures. The degradation of electronics is taken into account by replacing the initial energy values with re-calculated, distorted values, such that the reconstructed jet energy contains the footprints of the HEC electronics radiation damages, as explained below.

For each of four layers of the HEC, an average value of the expected neutron fluence has been used as presented in Figure 2. The actual value of the gain degradation factor, g_i, assigned to individual PAs in the PSB layer was randomly selected using a Gaussian function with parameters as presented in Table 3. The degraded measurement of the energy in each HEC sub-gap was calculated as $E' = E_{\text{init}} \cdot g_i$. The PA

16

Table 3: Average values of the HEC electronics degradation parameters.

PSB layer	n-fluence [n_{eq}/cm^2]	gain decrease factor, $\overline{g}$	non-linearity exponent, $\overline{p}$
0	$1.2 \cdot 10^{14}$	0.953 ± 0.008	1.006 ± 0.001
1	$7.1 \cdot 10^{13}$	0.972 ± 0.005	1.005 ± 0.001
2	$1.3 \cdot 10^{13}$	0.995 ± 0.002	1.004 ± 0.001
3	$3.8 \cdot 10^{12}$	0.998 ± 0.001	1.004 ± 0.001

output signals are summed actively by the summing stage of the ASIC and an overall calibration factor can be applied to the summed output. For a group of typically four summed PAs one correction coefficient $C_g = 4/(g_1 + g_2 + g_3 + g_4)$ was determined and applied to each of the four PAs individually, such that that $E'' = E' \cdot C_g$.

The signal non-linearity cannot be corrected by means of the HEC calibration system. A dedicated off-line method may however be developed in future to reduce the effect, but since typically four PAs are summed and only the summed signal can be corrected it is not possible to fully account for the degradation introduced by non-linearities.

The non-linearity effect was introduced in the simulation by taking into account the measured increase of the power-law exponent with the increase of radiation dose. The average values of selected degradation parameters are shown in Table 3. Again, a randomly selected non-linearity factor, p, was assigned to each PA and a new value of the deposited energy was calculated as $E_{degr} = (E'')^p E_{ref}^{(1-p)}$, where E_{ref} denotes a renormalization energy scale in order to equalize the visible energy before and after the degradation at the selected energy point. The choice of this reference scale is a bit arbitrary but should be in the range of typical energies measured in ATLAS for which it is assumed that the calibration factors restore the correct energy on average. In the analysis, the reference energy is once set to 100 GeV for all HEC layers and once to 5 GeV and 10 GeV, to account for different sampling fractions in front and rear longitudinal sections of the HEC, respectively.

Finally, the initial values of the deposited energy in every HEC sub-gap, E_{init}, were replaced in each event by the degraded values, E_{degr}, and the regular digitization and reconstruction algorithms were applied. The degraded pulse shape and autocorrelation functions corresponding to the assumed fluence values for each individual HEC channel were used in the digitization step instead of the default ATLAS values.

5.2 Simulation Results

Figure 18 shows results of the Monte-Carlo simulation for spectra of visible energy deposited in the LAr gaps and recorded in the front longitudinal HEC layer. The initial distribution (corresponding to E_{init}) is shown by black dots, whereas the histograms show results of the degradation algorithm applications, and the quoted numbers represent the average and RMS values of the corresponding distributions, respectively. The solid red line shows the visible energy spectrum obtained when considering gain and pulse shape degradation only (corresponding to E'' – i.e. corrected for the expected average gain loss). The comparison to the initial distribution shows that the calibration procedure can almost recover the
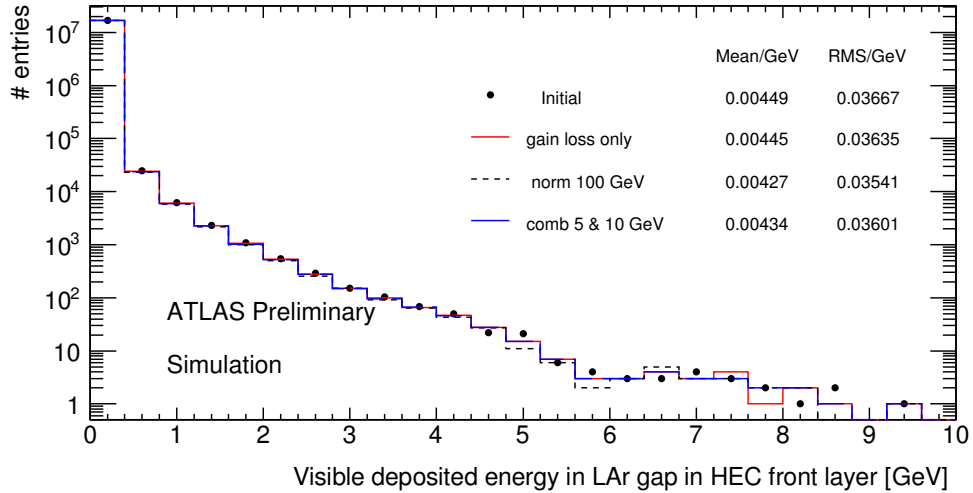
17

Figure 18: Distribution of the visible energy deposited in LAr gaps in the front HEC layer. The dots show the initial non-distorted distribution, the red histogram shows the effect of pulse-shape and gain degradation after correcting for the gain loss and the dashed and blue histograms the full degraded results with non-linearities taken into account for two choices of the reference energy scale for normalization.

degradation due to the PA's gain loss. The two other histograms demonstrate the final energy spectra (corresponding to E_{degr}) with non-linearities taken into account for two different normalizations performed at 100 GeV (dashed line) and at 5 and 10 GeV (blue solid line) for the front and rear longitudinal HEC segments, respectively. As expected, the normalization at the higher energy point results in lower visible energies, while the combined approach at lower energies provides better results when comparing to the initial distribution. The combined normalization is used from this point on.

The effect of electronics degradation on the HEC performance is very small as can be seen from the results shown in Figure 19. The jet performance plots show standard reconstructed anti-k_T jets with the distance parameter $R = 0.4$. The jets are constituted of calibrated topological clusters [32] and jet energy scale corrections [33] are applied. The top left plot in Figure 19 shows the energy distribution for the two leading jets in transverse momentum, reconstructed from the initial and degraded values of the deposited energy. One may note a shift of the degraded jet energy spectrum to lower values (in this case by ~0.5%).

Reconstructed jets were matched in $\Delta R = \Delta\eta \oplus \Delta\phi$ to Monte-Carlo jets at particle level (truth) by requiring $\Delta R < 0.4$. Distributions of the difference of reconstructed and truth jet energies were analysed for various truth jet energy intervals.

The energy dependence of the ratio of the RMS of the reconstructed jet energy over the mean reconstructed jet energy (jet energy resolution) is shown in Figure 19 (top right), whereas Figure 19 (bottom right) demonstrates the ratio between the mean reconstructed jet energy and the truth value (linearity) as a function of truth jet energy. The results are presented for initial and degraded jets. No significant change of the jet energy resolution is observed while the linearity degrades by ~ 0.5%. Also no significant degradation of the HEC performance is seen in Figure 19 (bottom left) where the initial transverse missing transverse momentum (MissingET) spectrum is compared to the degraded case. Larger deterioration of HEC PAs would affect the MissingET by introducing a tail with larger MissingET values – but at the radiation levels studied here this is not yet the case.
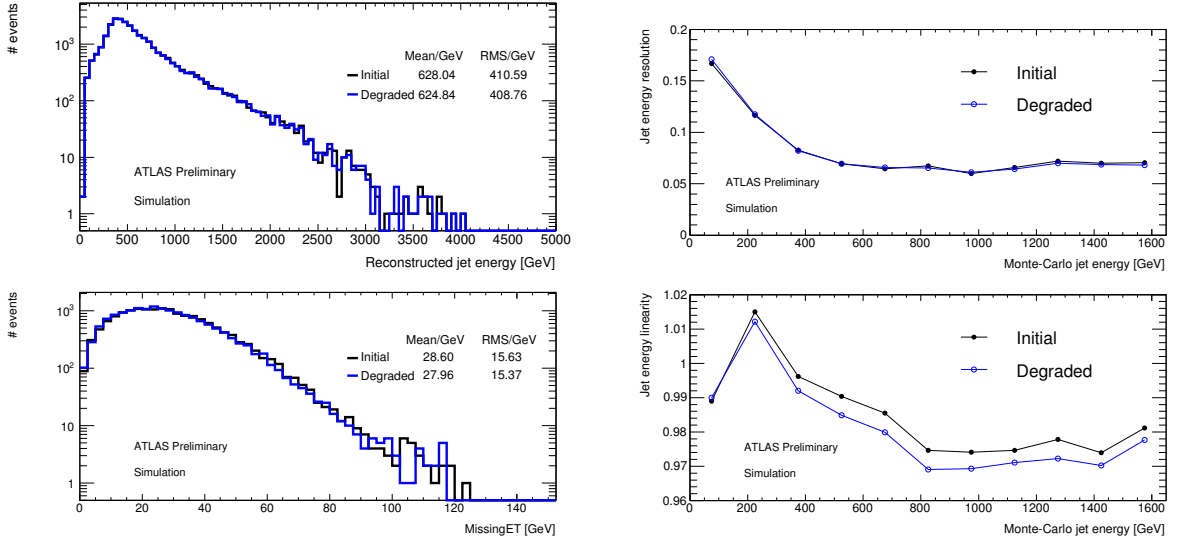
Figure 19: Summary of the electronics degradation on HEC performance: reconstructed jet energy spectra for calibrated anti-k_T jets with distance parameter $R = 0.4$ (top left); energy dependence of the jet energy resolution (top right) and relative non-linearity (bottom right); missing transverse momentum (MissingET) spectra (bottom left).

6 Irradiation Tests of Alternative Transistor Technologies

Together with the current HEC cold electronics new and potentially more radiation hard, alternative technologies were irradiated with neutrons at NPI and with protons at PSI. The three different transistor technologies tested were Si CMOS FET in SGB25V 250nm technology from IHP, SiGe Bipolar HBT (IHP SGB25V 250nm and IBM 8WLBiCMOS 130nm), and the GaAs FET currently used in ATLAS, either the Triquint CFH800 250nm transistors themselves (referred to as GaAs FET) or integrated into the HEC BB96 PAs and Systems (referred to as GaAs BB96).

6.1 Results

The various transistor parameters were calculated from the measured S-parameters using suitable small signal circuit models. The transistor parameters were averaged over a certain frequency range to obtain their mean and RMS-values for every set of S-parameters. This frequency range extended from 300 kHz to 100 MHz, unless a certain parameter was unstable at low or high frequencies, in which case appropriate cuts were applied. These averaged transistor values were then used to characterize their behaviour as a function of particle fluence.

Figure 20 summarizes the results for the proton (left) and the neutron (right) tests in terms of the appropriate gain parameters as a function of the corresponding particle fluence, normalized to the corresponding value before irradiation. The various gain parameters are the real part of the transconductance g_m for the FET transistors, the differential current gain β for the Bipolar transistors, and in case of the HEC BB96 PAs and systems, where simple transistor models are not applicable, the transresistance $r_m = \frac{\Delta V_{\text{out}}}{\Delta I_{\text{in}}} = |S_{21} \cdot Z_{\text{in}}|$, which relates the output voltage to the input current, where Z_{in} is the input impedance. Displayed are the sample averages of all the devices of a particular technology under test at
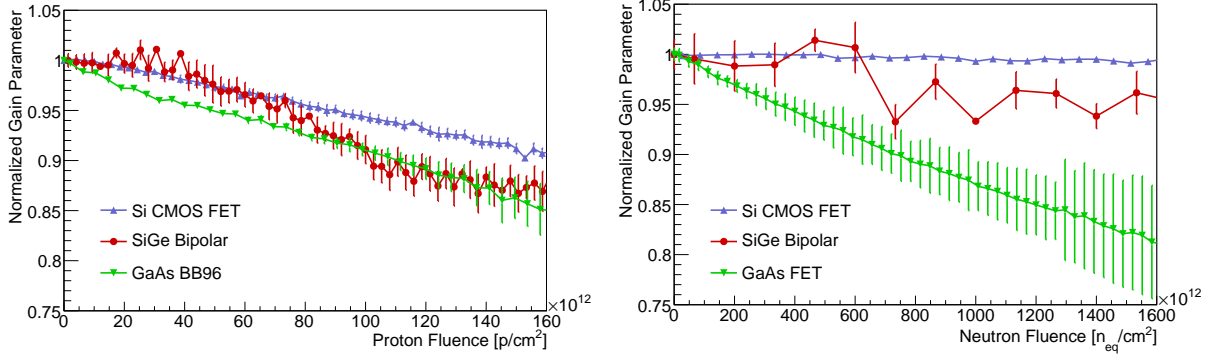
Figure 20: Relative gain loss as a function of proton (left) and neutron (right) fluence for the various technologies described in the legend. The respective gain parameters are described in the text. The data points represent the average of all the devices of a particular technology that were irradiated; the error bars are the sample RMS [34]. The neutron fluences are the 1 MeV equivalents for silicon as measured in Řež.

Table 4: Loss of gain of various transistor technologies under neutron and proton irradiation [34]. The neutron fluences are quoted for Si-NIEL in ATLAS. The total ionization dose (TID) was obtained from the proton fluence under the conservative assumption that proton irradiation causes damage only through ionization (TID, no NIEL). Measurements that have not been performed are labeled "n/a".

Technology	TID	Neutron fluence
	3.1 kGy	$1.2 \cdot 10^{14} \, n_{eq}/cm^2$
Si CMOS FET	0%	0%
SiGe Bipolar	0%	-1%
GaAs FET	n/a	-2%
GaAs BB96 (warm)	-1%	0%
GaAs BB96 (cold)	n/a	-5%

each of the two test facilities; the error bars represent the sample RMS. The relative change of the gain parameters up to the expected radiation doses for the HL-LHC (including a safety factor of 2) is quoted in Table 4. For the irradiations with 200 MeV protons the damage is assumed to stem from total ionization dose (TID) only, conservatively neglecting the NIEL damage. A TID of 3.1 kGy corresponds to a 200 MeV proton fluence of $5.4 \cdot 10^{12}$ p/cm^2 in Si and $7.3 \cdot 10^{12}$ p/cm^2 in GaAs [35].

6.2 Summary

The first observation is that even with an order of magnitude larger neutron flux, protons (or the TID they induce) would be the dominant cause of performance degradation for CMOS and SiGe transistors at the HL-LHC. In the case of the GaAs, the gain degradation is roughly the same for both types of irradiation, although a quantitative assessment suffers from the fact that two different gain parameters (transconductance for individual FETs versus transresistance for the BB96 ASIC) are being compared. For the neutron irradiation however, results for both the BB96 ASIC (see Section 3.5) and the individual

FETs are available and lead to 0% and 2% gain degradation in warm, respectively, at the HL-LHC fluences reported in Table 4.

It can be concluded that both the Si CMOS FETs and the SiGe Bipolar transistors considered as alternative technologies are more radiation hard than the currently used GaAs FETs. Among the alternative technologies, a preference would be given to the Si CMOS FETs, since the SiGe Bipolar transistors require a stabilization of their operation point, which would lead to a more complex circuitry. The effects of this unstable operation point can be seen in the larger fluctuations of the gain parameter as compared to the other two technologies.

7 Engineering of Installation

7.1 Replacement of HEC Cold Electronics and Installation of a New FCal

For the replacement of the HEC cold electronics the cryostat must be fully opened and the current FCal needs to be removed, i.e. the warm covers are removed on both faces, the inner tube including the FCal is lifted to surface and the cold covers are removed. To achieve this operation, access to both front and back faces of the cryostat is needed. The required configuration is shown in Figure 21; it allows the use of the crane to carry heavy equipment and tooling.
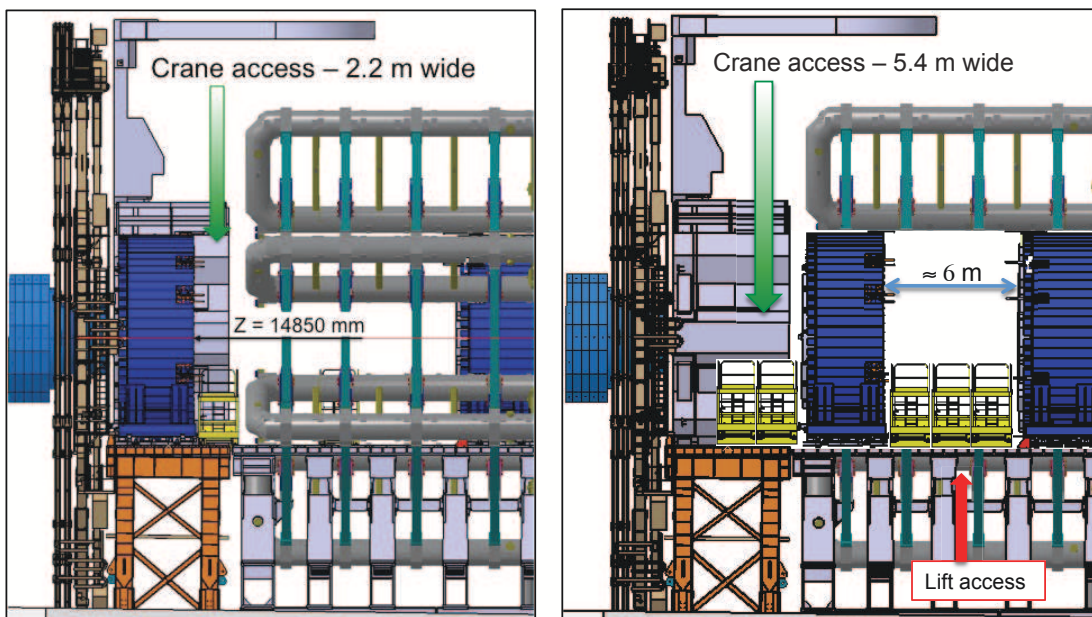

Figure 21: Cross section of half of the ATLAS experimental cavern. On the left figure the endcap calorimeter is in the temporary location to lower and install the needed tooling on the front face of the calorimeter. On the right side it is positioned to allow the FCal extraction and the HEC cold electronics replacement.

The cryostat is warmed up in parallel with the process of opening of the experiment. As a first step, the cryostat is moved back by approximately 11.5 m (to 14.850 m from the IP) so that a gap of ~2.2 m between the front face of the calorimeter and the barrel toroid is available. The mini-vans are installed at the front face of the cryostat, as well as the dedicated tooling for the FCal extraction. The existing neutron

shielding (JM moderator) is then removed, and finally the inner warm tube is dismounted. Afterwards the cryostat is moved towards the IP until its back face reaches 13.0 m from the IP, where the warm cover is removed. Then the special tooling named "Super-T6" is installed [36, 37].

7.2 Cryostat Opening and Closing / Cryogenics

One of the main technical issues is the opening of the cryostat. The cryostat is made of various parts: outer warm vessel, cold vessel, cold cover with inner bore for the FCal, cold bulkhead, inner cold tube, etc. The cold covers, on both faces, are welded. Therefore the welds must be cut to allow the opening of the cryostat (Figure 22), then the parts must be prepared to be welded together again. The cut of the welds of the various bulkheads of the cryostat will need some cutting machine, developed according to specific requirements concerning space and accessibility. Because of the radiation exposure, it may be necessary to operate this machine automatically or, at least, monitor it remotely.
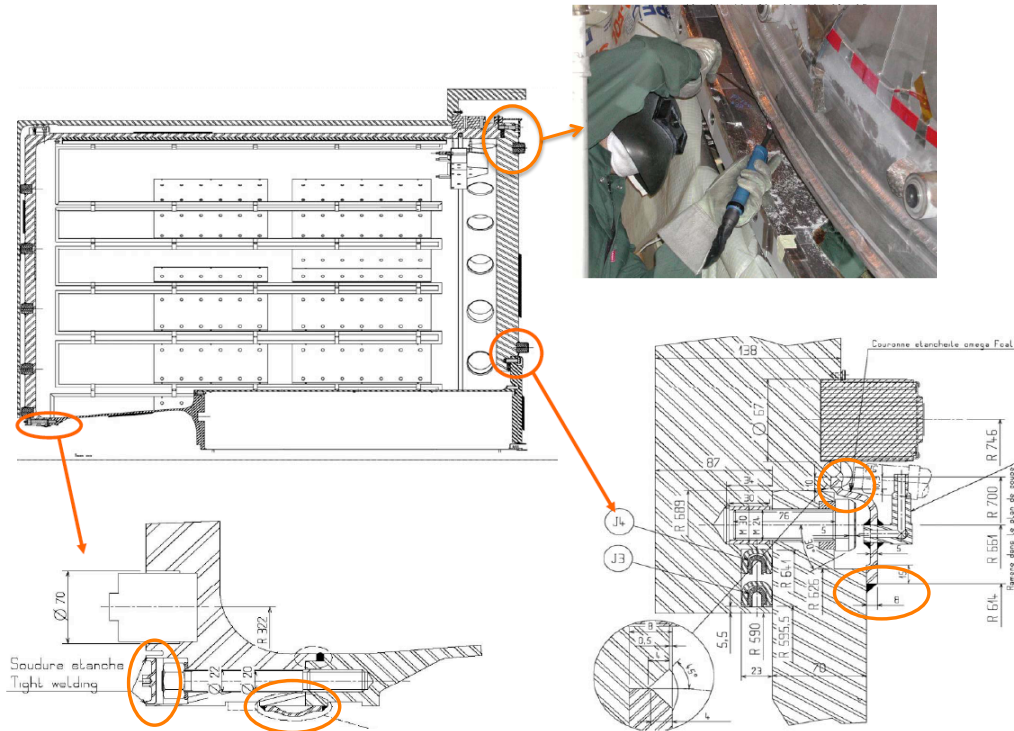

Figure 22: Details of the main welds closing the cryostat. Before removing the FCal, the welds at the inner bore on the front face and around the cold bulkhead on the back face must be cut. Moreover the removal of the cold cover requires cutting the weld all around the large radius.

The parts enclosing the FCal will be new ones. Regarding the large cold cover, which will be activated, a study must be performed to evaluate whether it can be refurbished or must be replaced. Some deformations of these components are expected due to the very low temperatures and subsequent ageing of material. Once the cold inner tube (enclosing the FCal) is released, the removal of the FCal is performed [38]. Some of the tools used at the time of the installation could be used again, with very few

modifications, however some tools have to be designed and manufactured for these procedures. They are mainly support frames and a mandrel to be inserted in the FCal inner bore. Some shielding components might be added to the support frames based on the results of the radiation protection analysis. These tools will have been installed beforehand as presented above. The mandrel will be aligned with respect to the inner bore of the cryostat. A guidance system will have to be part of the tooling. Afterwards, the FCal will be pulled out of the cryostat (Figure 23).
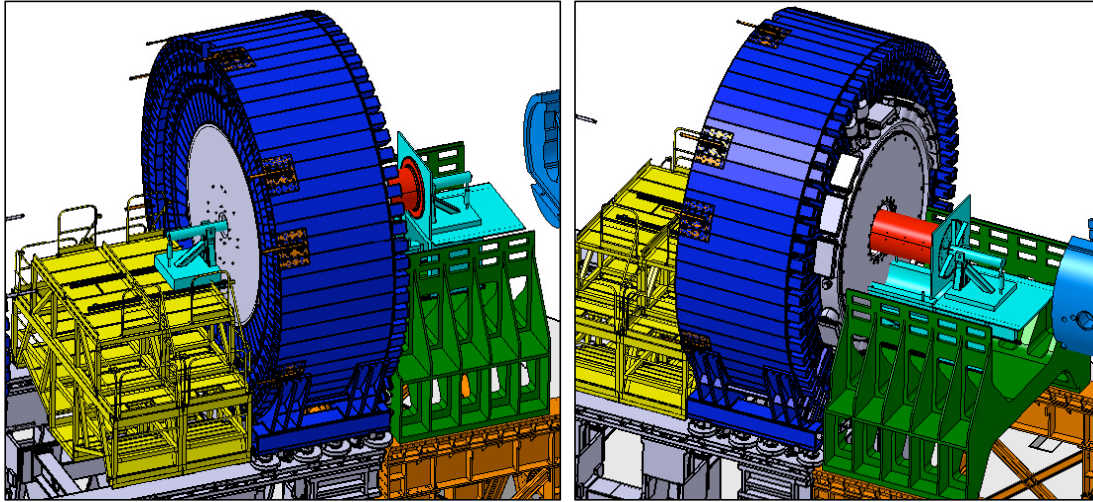

Figure 23: Extraction tooling of the FCal calorimeter inside the endcap cryostat. The FCal is clamped on a mandrel supported on each side of the calorimeter by moveable devices.

After a movement of the FCal by ~0.5 m, the cables will be accessible and it will be necessary to cut them before the full extraction can be done. Once extracted, the FCal will be housed in a shielded case and lifted by crane. Because the FCal summing boards are located behind the cryostat cold cover, they will not be accessible at this stage. After the cold cover removal, the extraction of the two HEC wheels will be done with the Super-T6. It has been designed as a large metallic structure, the main functions of which will be to extend the inner rails of the cryostat, on which the wheels are currently resting, and to provide means for the movement of the wheels (push/pull device). However, it will also provide suitable access to the HEC electronics boards and will support radiation shielding where necessary. In order to reduce time and radiation exposure of the personnel, these tools will be designed in an integrated fashion and will be easily installed. Moreover, it is necessary to include in the tooling a specific tent that could rest on the Super-T6 and would protect the detectors from dust and pollution (see Figure 24).

Finally, the HEC cold electronics will be accessible and can be replaced [39]. After the functional tests are performed successfully, the reverse tasks have to be carried out in order to push back the two HEC wheels, put back all cables and reconnect them. Afterward the replacement of the FCal summing boards will be done. Once this operation will be complete it will be possible to close the cryostat, to insert the new FCal into the cryostat inner bore, and finally to perform all vacuum and pressure tests needed to certify the cryostat before cool down.

7.3 Time Schedule

At the current state of the study, a tentative time schedule has been prepared [40]. The entire operation, including both the replacement of the HEC electronics and of the FCal, is estimated to last approximately 9 months per endcap, starting with the endcap calorimeter at warm temperature and at the right location. This estimate does not include the cool down time of the cryostats. In order to save time, activities on the second endcap are foreseen to start in the shadow of the first one, so that the operation on both sides could stay within 15 months.
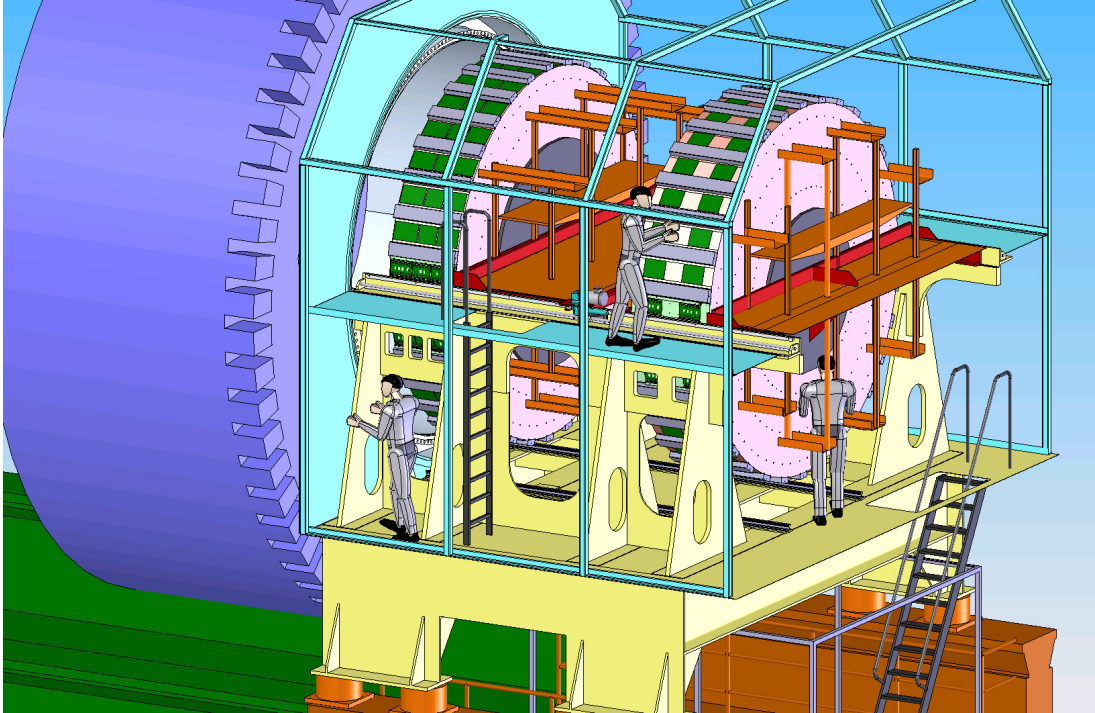

Figure 24: The two HEC wheels have been extracted from the cryostat. They are resting on the Super-T6 tooling.

8 Conclusion

The expected increase of the instantaneous (factor 7) and integrated (factor 3-5) luminosity of the HL-LHC with respect to the LHC has moderate consequences for the performance of the hadronic endcap calorimeter read-out electronics. Tests of potentially more radiation hard technologies were conducted in parallel with theses performance studies and procedures for the exchange of the cold electronics and the forward calorimeter have been evaluated. At this time, given the moderate performance impact expected, no intervention is planned.

References

[1] ATLAS Collaboration, Letter of Intent for the Phase-II Upgrade of the ATLAS Experiment, Tech. Rep. CERN-LHCC-2012-022. LHCC-I-023, CERN, Geneva (Dec 2012).
URL https://cds.cern.ch/record/1502664

[2] P. Krieger, Upgrade Plans for ATLAS Forward Calorimetry for the HL-LHC, Tech. Rep. ATL-LARG-PROC-2013-005, CERN, Geneva (Aug 2013).
URL https://cds.cern.ch/record/1595826

[3] D. Gingrich et al., Construction, assembly and testing of the ATLAS hadronic end-cap calorimeter, JINST 2 (2007) P05005. doi:10.1088/1748-0221/2/05/P05005.

[4] ATLAS Collaboration, The ATLAS Experiment at the CERN Large Hadron Collider, JINST 3 (2008) S08003. doi:10.1088/1748-0221/3/08/S08003.

[5] J. Bougher et al., A FLUGG-based Cavern background Simulation Application, Tech. Rep. ATL-COM-SOFT-2011-032, CERN, Geneva (Oct 2011).
URL https://cds.cern.ch/record/1394258

[6] S. Agostinelli et al., GEANT4: A Simulation toolkit, Nucl.Instrum.Meth. A506 (2003) 250–303. doi:10.1016/S0168-9002(03)01368-8.

[7] A. Ferrari et al., FLUKA: A multi-particle transport code (Program version 2005), Tech. Rep. CERN-2005-010, SLAC-R-773, INFN-TC-05-11, CERN, Geneva (2005).
URL https://cds.cern.ch/record/898301

[8] R. Engel, Photoproduction within the two component dual parton model. 1. Amplitudes and cross-sections, Z.Phys. C66 (1995) 203–214. doi:10.1007/BF01496594.

[9] ATLAS Collaboration, The ATLAS simulation infrastructure, Eur. Phys. J. C 70 (2010) 823–874. arXiv:1005.4568, doi:10.1140/epjc/s10052-010-1429-9.

[10] A. Ribon et al., Status of Geant4 hadronic physics for the simulation of LHC experiments at the start of LHC physics program, Tech. Rep. CERN-LCGAPP-2010-02, CERN, Geneva (2010).
URL http://lcgapp.cern.ch/project/docs/noteStatusHadronic2010.pdf

[11] T. Sjostrand, S. Mrenna, P. Z. Skands, A Brief Introduction to PYTHIA 8.1, Comput.Phys.Commun. 178 (2008) 852–867. arXiv:0710.3820, doi:10.1016/j.cpc.2008.01.036.

[12] S. Baranov et al., Estimation of Radiation Background, Impact on Detectors, Activation and Shielding Optimization in ATLAS, Tech. Rep. ATL-GEN-2005-001, CERN, Geneva (2005).
URL https://cds.cern.ch/record/814823

[13] R. Brun, F. Carminati, S. Giani, GEANT Detector Description and Simulation Tool, Tech. Rep. CERN-W5013, CERN-W-5013, CERN, Geneva (1994).
URL https://cds.cern.ch/record/1073159

[14] C. Zeitnitz, T. Gabriel, The GEANT - CALOR interface and benchmark calculations of ZEUS test calorimeters, Nucl.Instrum.Meth. A349 (1994) 106–111. doi:10.1016/0168-9002(94)90613-0.

[15] S. Menke, Proton and Neutron Irradiation Tests of Readout Electronics of the ATLAS Hadronic Endcap Calorimeter, MPP-2012-151 (2012). arXiv:1211.4060.
URL https://cds.cern.ch/record/1494974

[16] J. Ban et al., Cold electronics for the liquid argon hadronic end-cap calorimeter of ATLAS, Nucl.Instrum.Meth. A556 (2006) 158–168. doi:10.1016/j.nima.2005.10.114.

[17] GAFCHROMIC, GAFCHROMIC EBT2 Self-Developing Film for Radiotherapy Dosimetry, Tech. rep. (2009).
URL http://online1.ispcorp.com/_layouts/Gafchromic/content/products/ebt2/pdfs/GAFCHROMICEBT2TechnicalBrief-Rev1.pdf

[18] P. Bém et al., The NPI cyclotron-based fast neutron facility, Nucl.Data 2007 (2007) 555–558. doi:10.1051/ndata:07598.

[19] D. Dannheim, n-flux measurement Řež irradiation April 2010 (2010).
URL http://indico.mppmu.mpg.de/indico/getFile.py/access?contribId=3&resId=1&materialId=slides&confId=834

[20] K. Kurokawa, Power waves and the scattering matrix, IEEE Transactions on Microwave Theory and Techniques 13 (2) (1965) 194–202. doi:10.1109/TMTT.1965.1125964.

[21] Agilent Technologies, Specifying Calibration Standards and Kits for Agilent Vector Network Analyzers, Tech. Rep. 5989-4840EN (March 2011).
URL http://cp.literature.agilent.com/litweb/pdf/5989-4840EN.pdf

[22] L. Kurchaninov, Modeling of the HEC Electronics Chain, ATLAS HEC-Note-109 (2001).
URL https://wwwatlas.mpp.mpg.de/HEC_notes/hec109/hec109.pdf

[23] A. Vasilescu, G. Lindstroem, Displacement damage in silicon.
URL http://sesam.desy.de/members/gunnar/Si-dfuncs.html

[24] P. Griffin et al., SNL RML Recommended Dosimetry Cross Section Compendium, SAND92-0094 (1993).
URL http://dx.doi.org/10.2172/10115441

[25] A. Konobeyev, Y. Korovin, V. Sosnin, Neutron displacement cross-sections for structural materials below 800 MeV, J.Nucl.Mater. 186 (1992) 117–130. doi:10.1016/0022-3115(92)90328-I.

[26] G. Summers et al., Damage correlations in semiconductors exposed to gamma, electron and proton radiations, IEEE Trans.Nucl.Sci. 40 (1993) 1372–1379. doi:10.1109/23.273529.

[27] M. Huhtinen, P. Aarnio, Pion induced displacement damage in silicon devices, Nucl.Instrum.Meth. A335 (1993) 580–582. doi:10.1016/0168-9002(93)91246-J.

[28] A. Ougouag et al., Differential displacement kerma cross sections for neutron interactions in Si and GaAs, IEEE Trans.Nucl.Sci. 37 (1990) 2219–2228. doi:10.1109/TNS.1990.574218.

[29] A. Barry et al., The energy dependence of lifetime damage constants in GaAs LEDs for 1-500 MeV protons, IEEE Trans.Nucl.Sci. 42 (1995) 2104–2107. doi:10.1109/23.489259.

[30] T. Sjostrand, S. Mrenna, P. Z. Skands, PYTHIA 6.4 physics and manual, JHEP 0605 (2006) 026. arXiv:hep-ph/0603175, doi:10.1088/1126-6708/2006/05/026.

[31] M. Cacciari, G. P. Salam, G. Soyez, The anti-k_t jet clustering algorithm, JHEP 04 (2008) 063. arXiv:0802.1189, doi:10.1088/1126-6708/2008/04/063.

[32] T. Barillari et al., Local hadronic calibration, Tech. Rep. ATL-LARG-PUB-2009-001-2, CERN, Geneva (2008).
URL http://cdsweb.cern.ch/record/1112035

[33] ATLAS Collaboration, Jet energy measurement with the ATLAS detector in proton-proton collisions at $\sqrt{s}$ = 7 TeV, Eur.Phys.J. C73 (2013) 2304. arXiv:1112.6426, doi:10.1140/epjc/s10052-013-2304-2.

[34] H. Oberlack et al., Upgrade of the cold electronics of the ATLAS HEC calorimeter for sLHC generic studies of radiation hardness and temperature dependence, Nuclear Science Symposium Conference Record (NSS/MIC), 2009 IEEE (2009) 758–762. doi:10.1109/NSSMIC.2009.5402221.

[35] K. Olive et al., Review of Particle Physics, Chin.Phys. C38 (2014) 090001. doi:10.1088/1674-1137/38/9/090001.

[36] R. Langstaff, Tooling specification for a HEC wheel electronics replacement cradle, Tech. Rep. ATU-SYS-ES-0011, CERN (2010).
URL https://edms.cern.ch/document/1175049

[37] R. Langstaff, Installation procedure for the Super T6 HEC wheel tooling cradle in the ATLAS cavern, Tech. Rep. ATU-SYS-IP-0001, CERN (2011).
URL https://edms.cern.ch/document/1175051

[38] M. Raymond, M. Cadabeschi, Detailed procedure for cryostat opening and FCal extraction, Tech. Rep. ATU-SYS-EY-0001, CERN (2011).
URL https://edms.cern.ch/document/1175027

[39] S. Vogt, Exchange of the LAr HEC PSB boards: table for ALARA analysis, Tech. Rep. ATU-SYS-EY-0002, CERN (2009).
URL https://edms.cern.ch/document/1175036

[40] M. Raymond, Time schedule for option 1 installation: HEC electronics and FCal replacement, Tech. Rep. ATU-SYS-SC-0003, CERN (2010).
URL https://edms.cern.ch/document/1096695